Spatial deterministic wave forecasting for nonlinear sea–states

M. Galvagno,[1] D. Eeltink,[2,3] and R. Stuhlmeier[1]

[1])*Centre for Mathematical Sciences, University of Plymouth, PL4 8AA Plymouth, UK*

[2])*Department of Mechanical Engineering, Massachusetts Institute of Technology, Cambridge MA 02139-4307, USA*

[3])*Department of Engineering Science, University of Oxford, Oxford OX1 3PJ, UK*

(*Electronic mail: raphael.stuhlmeier@plymouth.ac.uk)

(Dated: 1 October 2021)

We derive a simple algebraic form of the nonlinear wavenumber correction of unidirectional surface gravity waves in deep water, based on temporal measurements of the water surface and the spatial Zakharov equation. This allows us to formulate an improvement over linear deterministic wave forecasting with no additional computational cost. Our new formulation is used to forecast both synthetically generated as well as experimentally measured seas, and shows marked improvements over the linear theory.

I. INTRODUCTION

The goal of deterministic wave forecasting is to determine what waves will arrive at a distant point, or at some future time, based on spatial or temporal measurements of the sea surface. To any beachgoer observing the erratic nature of surface water waves this may seem an impossible task, recalling Lord Rayleigh's famous statement that "The basic law of the sea way is the apparent lack of any law".

However, with advances in the remote sensing of the sea surface, and attendant increases in computational power, the problem of deterministic forecasting of water waves has become more tractable. The many applications of such deterministic forecasts – from control of wave energy converters[17,24], to ship motion forecasting for maritime operations[2,22] – have led to a significant surge in interest.

In the present work we set out to develop the theoretical basis of a forecasting methodology that incorporates weakly nonlinear corrections to the dispersion relation up to third order. While deep water waves undergo (nearly) resonant interactions at third and higher orders, it is our goal to capture only the corrected dispersion while neglecting the slow energy exchange between wave modes. In order to compare with wave flume experiments, we consider unidirectional spatial evolution, and build our theory upon the spatial Zakharov equation developed by Shemer et al[30] and employed in numerous subsequent studies[19,29,31].

Measurements of the free surface readily yield Fourier amplitudes, which form the basis of the linear description of surface waves. Indeed, these Fourier amplitudes can be used to construct simple and efficient linear forecasts, which have been used in practical tests of deterministic forecasting systems by Hilmer & Thornhill[15], Kusters et al[21], Al-Ani et al[2], and others. The same Fourier amplitudes are the foundation of weakly nonlinear approaches, where corrections to the linear description are sought as perturbations in the (small) wave slope.

Weakly nonlinear approaches to wave forecasting include those based on PDEs like the nonlinear Schrödinger equation and its modifications, derived under assumptions of narrow bandwidth and used by numerous authors, including Trulsen[36], Simanesew et al[32], Klein et al[20] and others. Alternatively, the well developed higher-order spectral method (HOS)[8,38] presents an attractive computational technique which has gained much recent attention by the deterministic forecasting community[4,13,23,28,39].

While they better capture the evolution of real waves, the principal drawback of these approaches lies in an increased computational cost compared to linear forecasting. For practical applications, forecasts are needed on scales of seconds or minutes and tens or hundreds of meters, so computational speed is of the essence. Our approach is to extract the correct third-order nonlinear dispersion and include it as an essentially algebraic correction in the linear forecast. This is computationally trivial, but we will show that it yields significant advantages over the purely linear approach.

In what follows, we first review fundamental theory, including linear forecasting, in section II A. Section II B 1 introduces the spatial Zakharov equation, and contains the main theoretical results. Section III applies linear and nonlinear forecasting methods to synthetically generated seas, simulated in a numerical wave flume using HOS. Section IV presents comparisons with experimental measurements. Finally, section V presents a discussion of the results and some concluding remarks. Additional data is provided in tables in the Appendix.

II. FUNDAMENTAL THEORY

Assuming unidirectional propagation of long-crested waves, we may write the free surface elevation as $\eta(x,t)$ where x is space and t time. In order to prepare a spatial forecast the sea surface must be measured at a fixed location $x = x_0$ at N times $t_0, t_1, \dots t_{N-1}$. It is simplest to assume time intervals $\Delta t = T/N$, where T is the measurement duration, so that $t_n = nT/N$, but non-uniformly sampled data can be resampled using interpolation. This leads to a record

$$y_0 = \eta(x_0,t_0), y_1 = \eta(x_0,t_1), \dots, y_{N-1} = \eta(x_0,t_{N-1}).$$

Taking the discrete-time Fourier transform of the sequence $y_0, y_1, \dots, y_{N-1}$ we find

$$Y_j = \sum_{n=0}^{N-1} y_n \exp(-i2\pi jn/N) = \sum_{n=0}^{N-1} y_n \exp(-it_n\omega_j), \tag{1}$$

where $\omega_j = 2\pi j/T$. We can obtain a continuous, periodic extension of the signal from the inverse transform, which can be written for N even as

$$y(t) = \frac{Y_0}{N} + \frac{1}{N}\sum_{m=1}^{N/2-1} \left[Y_m \exp(i\omega_m t) + Y_m^* \exp(-i\omega_m t)\right]. \tag{2}$$

Note that $y(t) = y(t+T)$. The term $Y_0/N = \frac{1}{N}\sum_{n=0}^{N-1} y_n$ is the mean elevation of the sampled points.

A. Linear forecasting

In the linear theory of gravity water waves there is a one-to-one correspondence between positive wavenumbers $k \in \mathbb{R}^+$ and positive frequency $\omega \in \mathbb{R}^+$, given by the dispersion relation

$$\omega^2 = gk \tanh(kd),$$

where g is the acceleration of gravity and d is the (constant) water depth. For deep water $d \to \infty$ this dispersion relation reduces to the simpler expression $\omega^2 = gk$. This correspondence allows for a linear forecast to be constructed from the N samples captured in (2). By stipulating that a wave with measured frequency ω_m has wavenumber $k_m = \omega_m^2/g$, it is immediately possible to write:

$$\zeta_L(x,t) = \frac{Y_0}{N} + \frac{1}{N}\sum_{m=1}^{N/2-1}\left[Y_m \exp(i(k_m x - \omega_m t)) + Y_m^* \exp(-i(k_m x - \omega_m t))\right]. \tag{3}$$

The waves accounted for in the forecast then have frequencies between $\omega_1 = \frac{2\pi}{T}$ and $\omega_{N/2-1} = 2\pi(N/2-1)/T$. The energy associated with a given frequency moves at the group velocity, defined as

$$c_g := \frac{d\omega(k)}{dk},$$

with the simple form in deep water $c_g = 0.5g/\omega$.

For a given measurement, the longest waves of interest ω_L will travel fastest, and the shortest waves ω_S slowest (note that practically ω_L may not be ω_1, nor ω_S be $\omega_{N/2-1}$, as there may be negligible energy associated with the longest or shortest waves that can be theoretically resolved). This leads to the concept of a predictable region in (x,t) as shown in Figure 1.

The thick lines in Figure 1 show the group velocities $c_{g,L}$ and $c_{g,S}$ of the longest and shortest waves ω_L and ω_S, respectively. Thinner lines in between these indicate the group velocities of waves of length intermediate between ω_L and ω_S. For a measurement at $x = 0$ over time $t = [t_0, t_1]$, all the waves in the shaded region originate in the measurement domain, and are therefore *predictable.* The only exceptions are waves longer than ω_L or shorter than ω_S that may encroach from $t < t_0$ or $t > t_1$, and are not accounted for in the forecast.

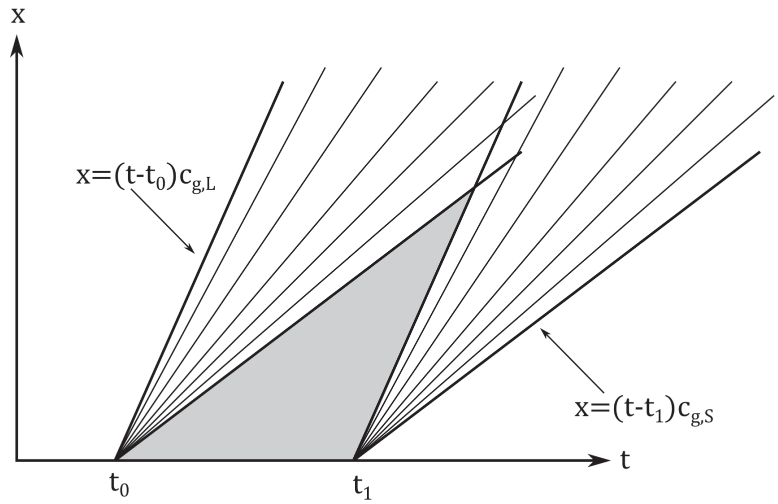

FIG. 1. Predictable region (grey shaded area) based on measurements at $x = 0$ in $[t_0, t_1]$.

B. Nonlinear forecasting

1. The spatial Zakharov equation

The discussion in the preceding section II A is relevant only for waves of small steepness, such that linear wave theory may be employed. Weakly nonlinear theory (to third order) makes for dramatic changes to the dispersion relation of waves in deep water, and complicates the forecast problem considerably.

The theoretical basis for our nonlinear forecast will be the spatial Zakharov equation (ZE) developed in the early 2000s by Shemer et al[30]. This takes the form

$$ic_g \frac{\partial B(x,\omega)}{\partial x} = \iiint T(k,k_1,k_2,k_3) B^*(x,\omega_1) B(x,\omega_2) B(x,\omega_3) \\ \cdot \exp(-i(k+k_1-k_2-k_3)x)\delta(\omega+\omega_1-\omega_2-\omega_3)d\omega_1 d\omega_2 d\omega_3. \tag{4}$$

where c_g denotes the deep-water, linear group velocity. This equation can be discretised as follows:

$$ic_{g,j} \frac{dB_j(x)}{dx} = \sum_{l,m,n} T_{jlmn} B_l^* B_m B_n \exp(-i(k_j+k_l-k_m-k_n)x)\delta(\omega_j+\omega_l-\omega_m-\omega_n), \tag{5}$$

where $B_i = B(\omega_i, x)$, and we abbreviate by T_{jlmn} the kernel $T(k_j, k_l, k_m, k_n)$ of the Zakharov equation. In (5) the function δ is the ordinary Kronecker delta function. To extract the effect of nonlinear dispersion we follow the procedure outlined by Stuhlmeier & Stiassnie[34] for the conventional temporal Zakharov equation (see also the discussion in Gao et al[11] for further background).

We write the complex amplitude $B_j(x)$ as $|B_j|\exp(i\arg B_j)$, where both magnitude and argument may depend on x. Separating into real and imaginary parts leads to:

$$c_{g,j}\frac{d|B_j|}{dx} = -\sum T_{jlmn}\delta_{jl}^{mn}|B_l||B_m||B_n|\sin(\theta_{jlmn}), \tag{6}$$

$$-c_{g,j}|B_j|\frac{d\arg(B_j)}{dx} = \sum T_{jlmn}\delta_{jl}^{mn}|B_l||B_m||B_n|\cos(\theta_{jlmn}), \tag{7}$$

with

$$\begin{aligned}
&\theta_{jlmn} = \Delta x + \arg B_j + \arg B_l - \arg B_m - \arg B_n,\\
&\delta_{jl}^{mn} = \delta(\omega_j + \omega_l - \omega_m - \omega_n), \text{ and}\\
&\Delta = k_j + k_l - k_m - k_n.
\end{aligned}$$

Assuming that there is negligible evolution of the amplitudes, so that the $|B_j|$'s may be replaced by their initial values $|B_j(0)|$, we rewrite

$$-c_{g,j}\frac{d}{dx}(\arg B_j) = \frac{1}{|B_j|}\left(\sum_l e_{lj}|B_l|^2|B_j|T_{jljl} + \sum_l\sum_{m\neq j}\sum_{n\neq j} T_{jlmn}\delta_{jl}^{mn}|B_l||B_m||B_n|\cos(\theta_{jlmn})\right) \tag{8}$$

and, neglecting the second term on the right-hand side (which captures only exactly resonant quartets), integrate:

$$-c_{g,j}(\arg B_j) = \sum_l e_{lj}|B_l|^2 T_{jljl}x + \arg B_j(0), \tag{9}$$

where $e_{lj} = 1$ for $l = j$ and $e_{lj} = 2$ for $l \neq j$. The kernels of the Zakharov equation reduce for two unidirectional waves (scalar k) to

$$T(k,k_1,k,k_1) = \begin{cases} \frac{kk_1^2}{4\pi^2} & \text{for } k_1 < k,\\ \frac{k^2k_1}{4\pi^2} & \text{for } k_1 \geq k. \end{cases} \tag{10}$$

This leads to a correction for the wavenumber:

$$K_n = k_n - \frac{1}{c_{g,n}}\sum_l e_{ln}|B_l(0)|^2 T_{lnln}, \tag{11}$$

which is the counterpart to the well-known Stokes' correction to the frequency. The effects of (weak) nonlinearity are thus to decrease the wavenumber by an amount of $O(\varepsilon^2)$ compared to the linear theory. We will explore the effect of this wavenumber correction on two explicit solutions below, and see that it also impacts the predictable region discussed in section II A above.

2. *Explicit solutions to the spatial Zakharov equation*

The spatial Zakharov equation (4) can be easily solved in two special cases: a single mode, or two modes. The former corresponds to the spatial evolution of the well-known Stokes' wave[33], and the latter to the spatial evolution of the third-order two-wave system first considered by Longuet-Higgins & Phillips[25]. Either of these cases trivially fulfil the resonance condition, since $\delta(\omega_a+\omega_a-\omega_a-\omega_a)=1$ and $\delta(\omega_a+\omega_b-\omega_a-\omega_b)=1$. Because the viewpoint of wavenumber correction (rather than frequency correction) is somewhat unusual in water waves, it is instructive to consider these solutions.

In case of a single wave ω_j, the spatial Zakharov equation (with T_{jjjj} abbreviated by T_j) becomes

$$ic_{g,j}\frac{dB_j(x)}{dx}=T_j|B_j(x)|^2B_j(x), \tag{12}$$

which admits the constant amplitude solution

$$B_j(x)=A_je^{-iA_j^2T_jx/c_{g,j}}. \tag{13}$$

If two waves are present, say ω_a and ω_b, the spatial ZE becomes the coupled system

$$ic_{g,a}\frac{dB_a}{dx}=T_a|B_a|^2B_a+2T_{ab}|B_b|^2B_a, \tag{14}$$
$$ic_{g,b}\frac{dB_b}{dx}=T_b|B_b|^2B_b+2T_{ab}|B_a|^2B_b, \tag{15}$$

where the symmetry of the kernel $T_{abab}=T_{abba}$ has been used to simplify the expressions and T_{abab} has been abbreviated by T_{ab}. Again, this system admits a solution with constant amplitudes A_a and A_b,

$$B_a(x)=A_a\exp(-i(T_aA_a^2+2T_{ab}A_b^2)x/c_{g,a}), \tag{16}$$
$$B_b(x)=A_b\exp(-i(T_bA_b^2+2T_{ab}A_a^2)x/c_{g,b}). \tag{17}$$

The relationship between the complex amplitudes and the leading order free surface elevation is given by

$$\eta(x,t)=\frac{1}{2\pi}\int_{-\infty}^{\infty}\left(\frac{\omega}{2g}\right)^{1/2}[B(x,\omega)\exp(i(k(\omega)x-\omega t))+\text{c.c.}]\,d\omega. \tag{18}$$

Here "c.c." stands for the complex conjugate of the preceding expression. For a single mode $B(x,\omega)=B_0(x)\delta(\omega-\omega_0)$ we find, using (13),

$$\eta(x,t) = \frac{1}{\pi}\left(\frac{\omega_0}{2g}\right)^{1/2} A_0 \cos(([k(\omega_0) - A_0^2 T_{0000} x/c_{g,0}]x - \omega_0 t)). \tag{19}$$

This is a simple sinusoidal wave with a wavenumber altered due to the effect of the weakly nonlinear dispersion relation. Normalising the constant amplitude via

$$A_0 = \pi a_0 \left(\frac{2g}{\omega_0}\right)^{1/2},$$

this reduces to

$$\eta(x,t) = a_0 \cos(k_0[1 - a_0^2 k_0^2]x - \omega_0 t).$$

An exactly analogous procedure for two waves ($k_a < k_b$) yields the free surface

$$\eta(x,t) = a_a \cos\left(k_a\left[1 - a_a^2 k_a^2 - 2a_b^2 k_a^{3/2} k_b^{1/2}\right] x - \omega_a t\right) + a_b \cos\left(k_b\left[1 - a_b^2 k_b^2 - 2a_a^2 k_a^{3/2} k_b^{1/2}\right] x - \omega_b t\right).$$

This shows clearly that the dispersion of one mode ω_a is influenced both by its own steepness a_a and also by that of the second mode ω_b. It is easy to verify that these wavenumber corrections can be obtained from equation (11), making liberal use of (10) to simplify the kernels.

3. Nonlinear forecasts with wavenumber correction

The wavenumber correction (11) gives rise to a simple improved forecast

$$\zeta_N(x,t) = \frac{Y_0}{N} + \frac{1}{N}\sum_{m=1}^{N/2-1}\left[Y_m \exp(i(K_m x - \omega_m t)) + Y_m^* \exp(-i(K_m x - \omega_m t))\right], \tag{20}$$

where K_m denotes the corrected wavenumber. This is otherwise cosmetically identical to the linear forecast (3), a kinship which demonstrates the advantages of the formulation. Indeed, the only additional computational cost consists of calculating the K_m's from the Fourier amplitudes via simple algebra.

In addition, the change in wavenumber leads to a change in phase and group velocities, which become $c_{p,j} = \omega_j/K_j$ and $c_{g,j} = d\omega_j/dK_j$, respectively. The latter of these must be evaluated numerically in practice. The nonlinear corrected velocities are somewhat larger, effectively because of a smaller denominator (K_j is smaller than the linear wavenumber k_j, and this effect is more pronounced for shorter waves than for longer waves), which means that the spatial predictable zone increases in size slightly when nonlinear corrections are taken into account. The extent of this increase depends on both the frequencies and the amplitudes present in the measured sea.

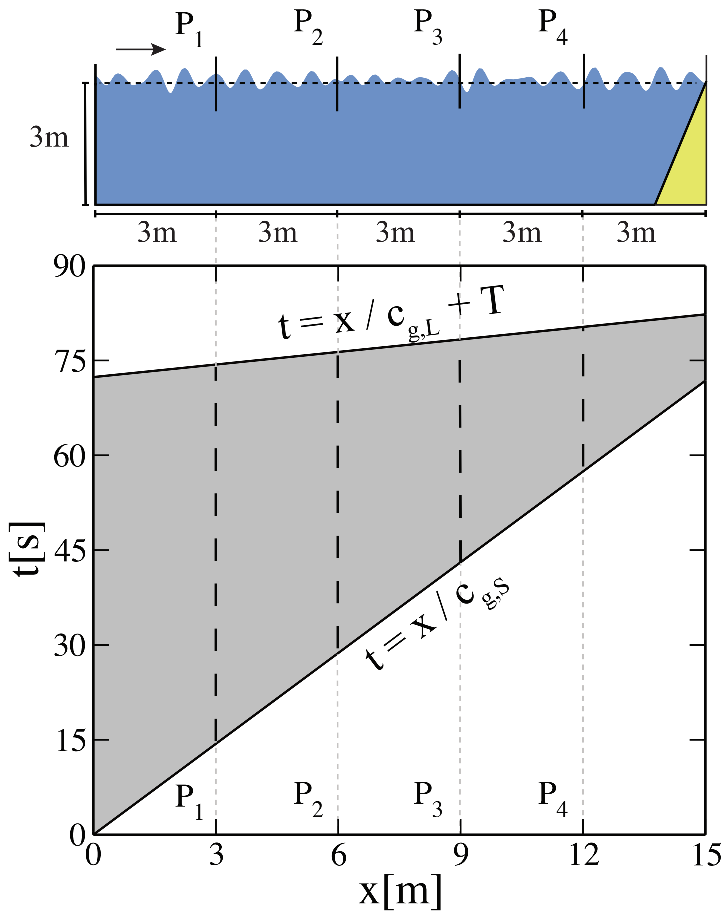

FIG. 2. The upper panel shows a diagram of the HOS-NWT numerical wave flume configuration. P_1–P_4 denote the probes at which measurements are taken. Right-going waves are generated in water of 3 m depth, and fully absorbed by a numerical beach at the right-hand side of the flume. The lower panel depicts the nonlinear predictable zone for a JONSWAP spectrum with $H_s = 0.03$ m, $\gamma = 3.3$ generated in the 15 m long HOS-NWT numerical wave flume. Waves are generated at the wavemaker ($x = 0$ m) between $t = 0$ and $t = T = 72$ s.

III. DETERMINISTIC FORECASTING OF SYNTHETIC SEAS

To assess the utility of the linear and the new nonlinear deterministic forecast it is necessary to generate a wave field, measure it at a point, and compare the forecast with other measurements. This procedure can be undertaken either in a wave flume or computationally, and we devote this section to the latter. The advantage of synthetic seas lies in the ease of tuning inputs, and the ability to easily produce many realisations of different cases. To this end, we employ the open source HOS-NWT code[9] which implements the high-order spectral method (HOS).

Throughout we use a numerical wave flume to generate purely unidirectional, random wave fields initialised by JONSWAP spectra with peak frequency $f_p = 1.3$ Hz, values of significant wave–height H_s between 0.02 – 0.04 m, and peak-sharpening parameters $\gamma = 1, 3.3$ and 7. The numerical wave flume is 15 m long and 3 m deep, with probes located at 3, 6, 9 and 12 m, and has a fully absorbing beach, as depicted in the upper panel of Figure 2. HOS is used to model the nonlinear propagation of waves along the flume, and includes nonlinear dispersion, (near) resonant energy exchange, and the effects of bound modes – considerably more physics than captured by either of our simple forecasts.

To produce a forecast, measurements from probe P_1 are sampled, the Fourier amplitudes extracted via FFT, and inserted into either (3) or (20). The resulting forecasts can then be compared to the measured time series at subsequent probes P_2, P_3, and P_4. The lower panel of Figure 2 depicts the nonlinear predictable zone based on an example for $H_s = 0.03$ and $\gamma = 3.3$. Waves are generated by the wavemaker at $x = 0$ m and propagate along the 15 m long numerical flume. The longest waves resolved are $\omega_L = 3.1\,\mathrm{rad}/s$ and the shortest $\omega_S = 25.1\,\mathrm{rad}/s$, and the associated nonlinear group velocities determine the edges of the predictable zone. The data at P_1 is then used to generate forecasts as shown in Figure 3. The horizontal (time) axis has a different starting point for each panel of Figure 3, reflecting the narrowing of the predictable region seen in Figure 2 (for convenience, in Figure 2 we have set $t = 0$ s as the beginning of the record at P_1, rather than the start of the wavemaker).

Figure 3 shows excellent agreement between measurement and both forecasts for the closest probe P_2, while the forecast grows progressively less accurate as distance from the measurement point increases. However, the nonlinear forecast ζ_N remains considerably closer to the measured data at P_4, some ten peak wavelengths from the initial measurement.

In order to obtain a measure of the aggregate quality of a forecast it is useful to compare the fit over several realisations. Figure 4 considers the mean correlation $\bar{\rho}$ (using Pearson's linear correlation coefficient ρ, where a value of $\rho = 1$ indicates that the two signals rise and fall together, and a value of $\rho = -1$ indicates that one rises when the other falls) between a linear or nonlinear forecast produced from probe 1 and the predictable portion of the measured time series at probe n, for $n = 2$, 3, or 4. Here and elsewhere the predictable region is calculated based on the nonlinear group velocities; it is therefore strictly slightly larger than the comparable predictable zone based on linear group velocities, see section II B 3.

Figure 4 has been generated by forecasting 20 realisations of a JONSWAP spectrum with $\gamma =$

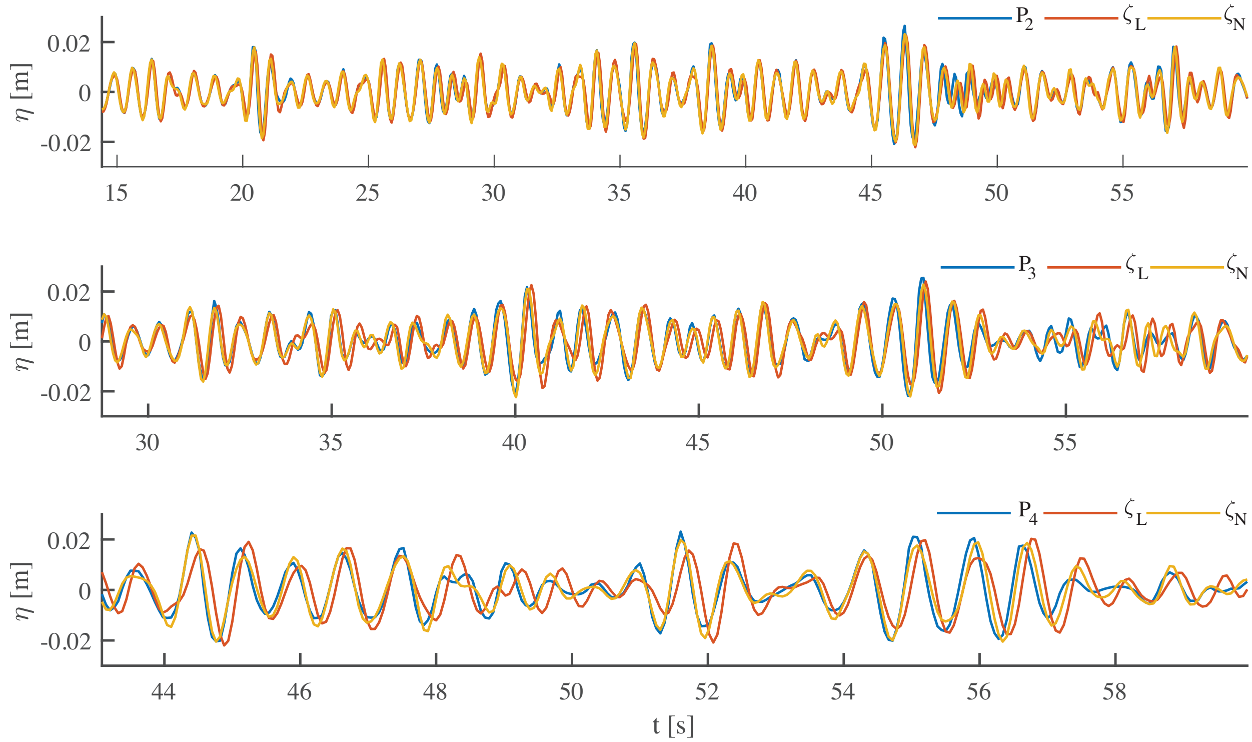

FIG. 3. Comparison of linear (ζ_L, red curve) and nonlinear forecasts (ζ_N, yellow curve) with measurements (P_i, blue curve) for a numerically generated JONSWAP spectrum with $H_s = 0.03$ and $\gamma = 3.3$. The horizontal axis shows time (a section through the nonlinearly corrected predictable region), while the vertical shows free surface elevation. (Top panel) comparison with measurements at probe P_2. (Middle panel) comparison with measurements at probe P_3. (Bottom panel) comparison with measurements at probe P_4.

3.3, each with random, uniformly distributed phases. Subsequently the arithmetic mean of the linear correlations is plotted: at the measurement point P_1 ($\Delta x = 0$ m) the forecast is identical to the probe record, yielding perfect correlation $\rho = 1$ in all cases. With distance Δx from the measurement, the average correlation is shown to decrease – markedly for steeper seas and linear forecasts (dashed lines), but much less so for the nonlinear forecast.

Table I in the Appendix provides the numerical values of the mean correlations for JONSWAP spectra with $\gamma = 1$, 3.3 and 7. As in Figure 4, for higher wave steepness, nonlinear dispersion is well captured by the corrected forecast ζ_N (see rows $\bar{\rho}^N_{i,j}$), as evidenced by the good agreement for moderate distances. Table II additionally provides the root-mean-square (RMS) error for each of the cases considered, which captures the error in amplitude as well as phase (in contrast to the correlation, which only captures the concurrent increase/decrease of two signals). It is remarkable that the nonlinear forecast at 9 m distance has nearly the same RMS error as the linear forecast at

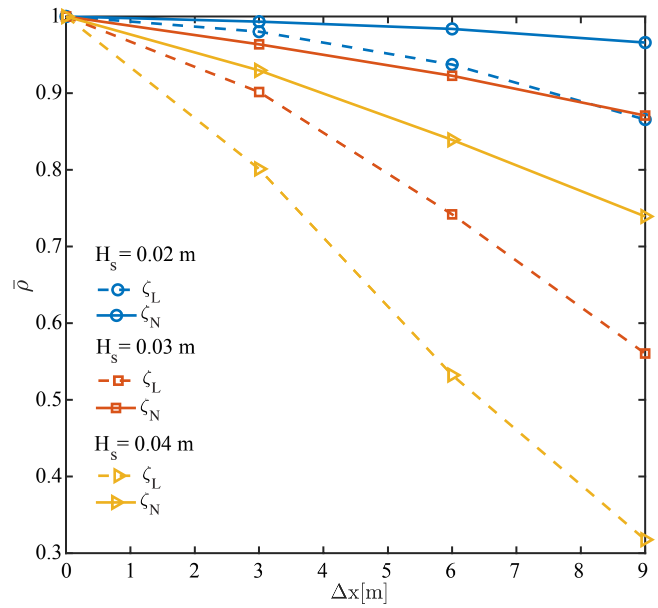

FIG. 4. Mean correlations $\bar{\rho}$ over 20 realisations between synthetic simulated seas and forecasts based on linear (ζ_L) and nonlinear (ζ_N) forecasts. The horizontal axis Δx denotes distance from the measurement probe P_1, and markers are placed at probes P_2, P_3 and P_4. Three difference significant wave heights H_s ranging from 0.02 to 0.04 are used, and peak-sharpening parameters $\gamma = 3.3$.

3 m for all cases considered.

For the steepest waves and longest propagation distances the forecast quality degrades markedly, nevertheless the nonlinear forecast retains a clear advantage in both correlation and RMS error. Indeed, for $H_s = 0.03$ and 0.04 m and over all values of γ, the nonlinear forecast can predict twice as far (6 m vs 3 m) as the linear forecast with the same average correlation and RMS error. It is also interesting to note that prediction is consistently easier for narrower spectra ($\gamma = 3.3, 7$), with accuracy of both linear and nonlinear forecasts increasing at a given distance as γ increases.

IV. DETERMINISTIC FORECASTING IN A WAVE FLUME

To assess the accuracy of our new nonlinear forecasting approach, we also compare with experimental data from the 40 m long, 2.7 m wide flume at IRPHE/Pytheas Aix Marseille University. Data are taken from four probes placed at distances of 3.79, 6.64, 11.63, and 16.11 m from a piston wave maker in water of depth $d = 0.8$ m, as shown in Figure 5. As above, measurements from probe 1 will supply the data necessary to produce a forecast, which is then compared with

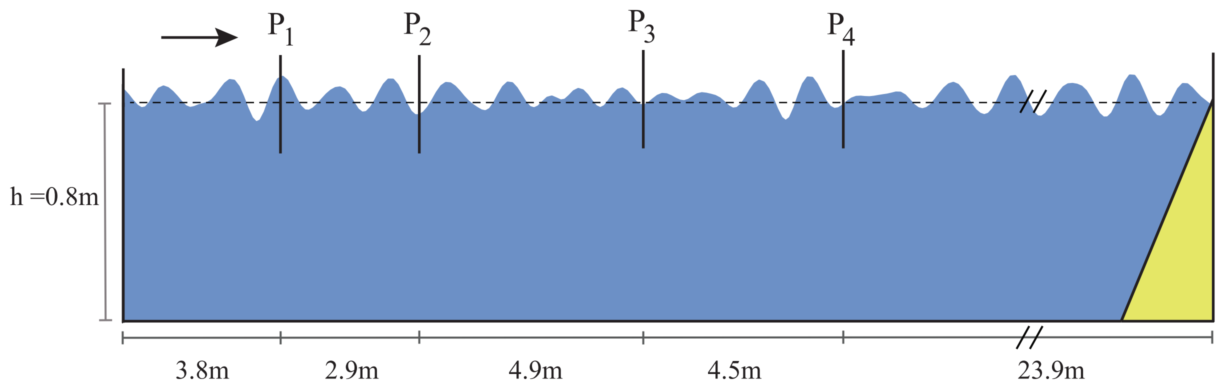

FIG. 5. Diagram of the experimental configuration. P_1–P_4 denote the probes at which measurements are taken. Right-going waves are generated in water of 0.8 m depth.

data from probes 2–4. We will consider three cases: (J1) a JONSWAP spectrum with $f_p = 1.10$ Hz, $\gamma = 3.3$ and $H_s = 0.01$ m, (J2) a steeper JONSWAP spectrum with $f_p = 1.11$ Hz, $\gamma = 3.3$ and $H_s = 0.04$ m, and (M) a modulated plane wave, consisting of a plane wave with $f_p = 1.42$ and slope $ak = 0.16$, and two side bands.

Forecasts for the two JONSWAP cases J1 and J2 are depicted in panel (a) and panel (b) of Figure 6 respectively. For lower steepness wave fields with $H_s = 0.01$ either linear or nonlinear forecasting produces excellent agreement with measurements up to probe P_3, nearly 8 m (ca. 7 peak wavelengths) away, as seen in Figure 6(a). Due to the low steepness, the nonlinear correction is essentially negligible, and ζ_L is barely distinguishable from ζ_N. Akin to what was observed for synthetic data generated by HOS in section III, as the wave steepness is increased to $H_s = 0.04$ m the forecasts begin to depart from the measured data. The difference in linear and nonlinear forecasts is clearer here, with the quality of the dispersion-corrected forecast ζ_N outstripping the simple linear case ζ_L. This information is also captured by the correlation, shown in Figure 8, and RMS error, shown in the Appendix, Table III, which provide a measure of forecast quality (here only over a single experimental realisation).

Forecasts for a modulated plane wave are shown in Figure 7. This case exhibits the well-known modulational instability of a degenerate quartet consisting of a carrier and two side bands, and the side-band growth with propagation distance can be clearly seen in the insets depicting the Fourier amplitude spectrum at probes P_2, P_3 and P_4. As the wave-field propagates along the flume, the side-band amplitudes grow at the expense of the carrier, while also influencing the modes' dispersion.

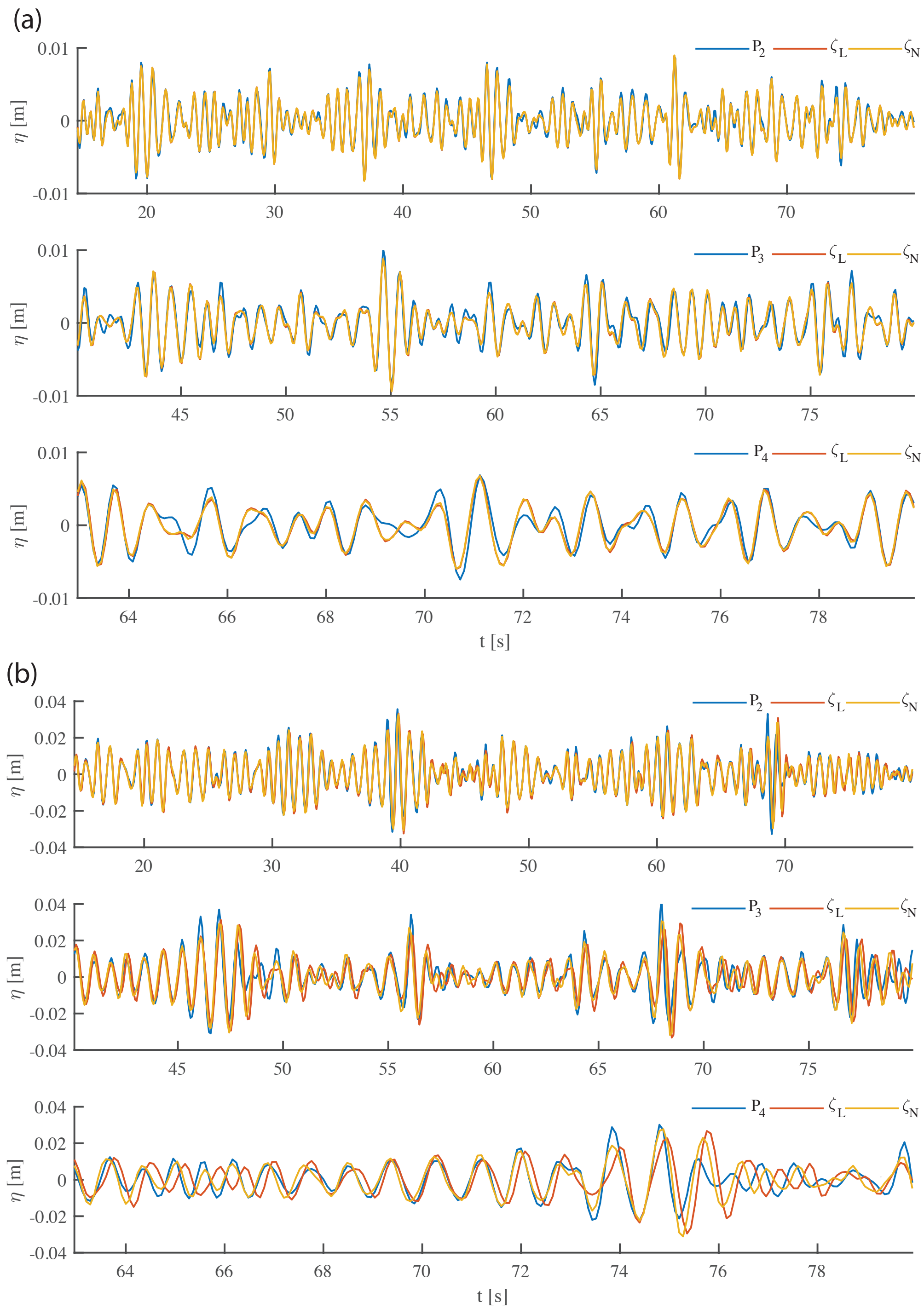

FIG. 6. Comparison of linear (ζ_L, red curve) and nonlinear (ζ_N, yellow curve) forecasts with measured probe data (P_i, blue curve) for JONSWAP cases J1 (panel (a)) and J2 (panel (b)). Measurements taken at probe P_1 supply the Fourier amplitudes for the forecasts at probe P_2 (top panel), probe P_3 (middle panel) and probe P_4 (bottom panel).

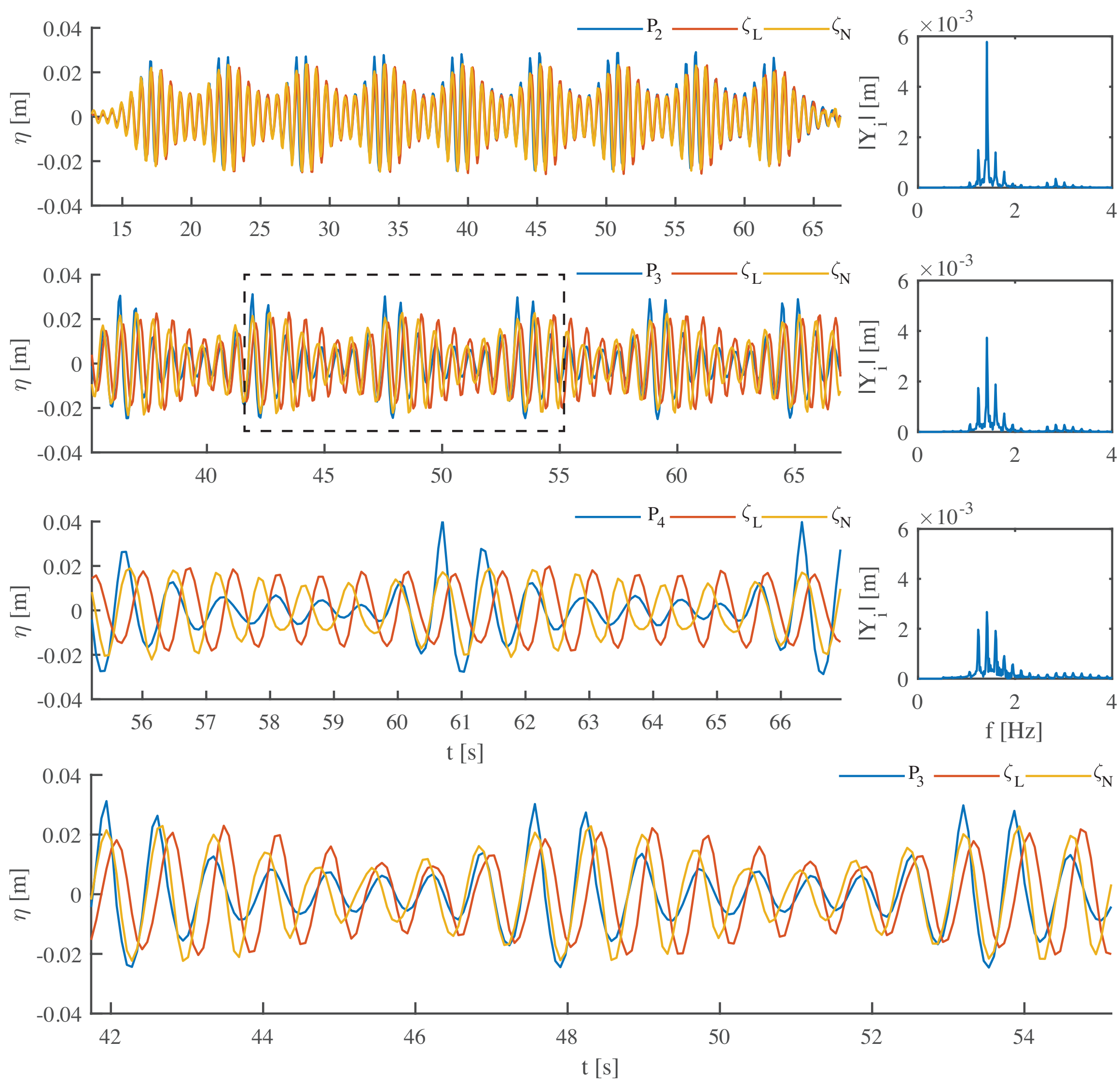

FIG. 7. Comparison of linear (ζ_L, red curve) and nonlinear (ζ_N, yellow curve) forecasts with measured probe data (P_i, blue curve) for modulated plane wave case M. Measurements taken at probe P_1 supply the Fourier amplitudes for the forecasts at probe P_2 (top panel, 2.85 m propagation distance), probe P_3 (second panel, 7.84 m propagation distance) and probe P_4 (third panel, 12.32 m propagation distance). The bottom panel is an enlargement of the region outlined in black in panel 2. The Fourier amplitude spectrum at the three measurement gauges P_2, P_3 and P_4 is shown adjacent to panels 1–3.

The nonlinear forecast ζ_N employs only the initial mode amplitudes to calculate the corrections to the dispersion relation (the procedure described in section II B 1 effectively neglects the energy exchange between modes, employing the Fourier amplitudes of P_1 throughout). The effect of this is clearly visible in the enlarged forecast in Figure 7 (bottom panel). It is also illustrated in Figure

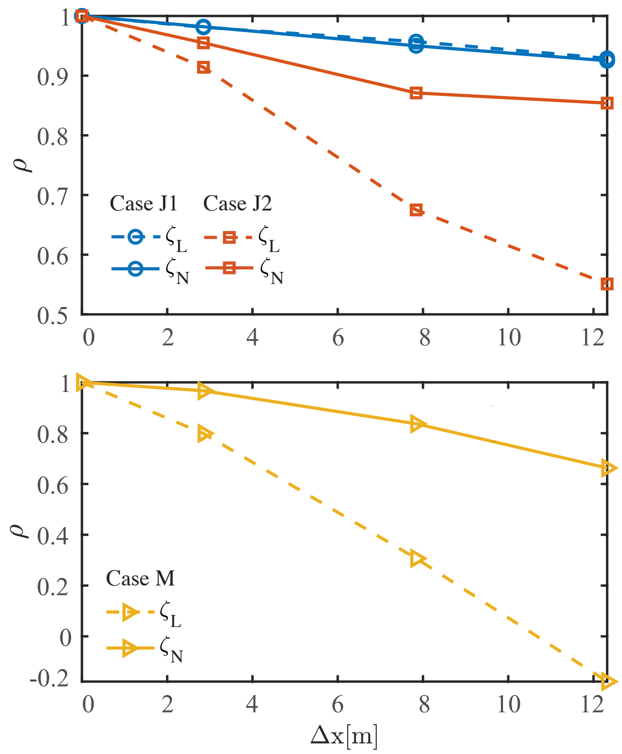

FIG. 8. Correlations ρ between experimental measurements and forecasts based on linear (ζ_L) and nonlinear (ζ_N) forecasts. The horizontal axis Δx denotes distance from the measurement probe P_1, and markers are placed at probes P_2, P_3 and P_4. Upper panel: JONSWAP cases $J1$ and $J2$. Lower panel: modulated plane wave case M.

8 which depicts the correlation between measurements and forecasts and Table III which gives the RMS errors: the nonlinear forecast ζ_N shows excellent agreement with the measured phases, but fails to capture the evolving amplitudes at larger distances. Because the correlation is insensitive to amplitudes, good agreement is found for all nonlinear forecasts up to probe P_4 in Figure 8. For yet longer propagation distances, the different rates of change of the various amplitudes eventually degrade the otherwise good match between the phases in ζ_N and the experimental record.

V. DISCUSSION

We have derived a compact and theoretically simple wavenumber correction from the spatial Zakharov equation, and demonstrated its utility in simple cases of wave forecasting from synthetic and experimentally generated waves. We have seen that this method accurately captures the most important aspects of nonlinear dispersion in one propagation direction, and is a spatial analogue of the techniques developed by Stuhlmeier & Stiassnie[35] for the temporal forecasting problem. In contrast to the temporal case, it remains a significant challenge to extend the spatial Zakharov formulation (and attendant wavenumber corrections) to directional (2D) seas. These corrections may have applicability beyond the immediate context of deterministic forecasting, for example to the so-called Molin lensing effect[26] which has recently been studied in the context of wave run-up[41].

Wave prediction theories, such as that presented in this manuscript, are only one part of this story: ocean waves must first be properly measured. For ship-borne applications, considerable work is currently being undertaken on X-band marine radar[27,42]. For fixed installations, such as wave energy converters, in-situ measurements may be obtained by Acoustic Doppler Current Profiler[17], arrays of inexpensive buoys[10], LiDAR[12], or stereo-imaging[40], to name only some of the many possibilities. There have also been recent mathematical advances[5,14] in recovering the free-surface from bottom pressure measurements, which may allow for practical exploitation. Measurement errors and sources of noise must be dealt with efficiently, as discussed recently by Desmars et al[7], for example by continuous data assimilation and ensemble Kalman filtering[37]. Subsequently prediction can be accomplished with a wide variety of propagation techniques.

We have used the fast Fourier transform throughout, and tacitly assumed that it introduces no appreciable errors into the forecasting methodology. This is not quite the case, as the sampled water surface is not a strictly periodic signal, and we have only a finite-length snapshot at each probe location. This induces a rectangular windowing and results in spectral leakage, recently addressed in the context of forecasting[1,16].

It is interesting to observe that in our synthetic forecasts a decrease in spectral width (by increasing γ) increases the average accuracy of our forecasts, as measured by the linear correlation and presented in table I. Of the two phenomena associated with cubically nonlinear wave propagation in deep water, energy exchange is expected to be more significant for a narrow spectrum, while frequency correction is expected to be less significant. The former phenomenon is connected to the Benjamin-Feir index introduced by Janssen[18], connecting spectral width and scale of nonlinearity to the appearance of modulational instability. The latter is a consequence of the asymmetry of (11): energy in long waves has a large effect on the dispersion of short waves, but not vice versa. For a broader spectrum, with energy distributed among modes further from the spectral peak (especially in higher frequencies), these dispersion corrections should therefore be more significant[34].

The extremely narrow and discrete spectrum of the modulated plane wave in Figure 7, allows to track energy transfer clearly, and makes it a popular laboratory wave, although it is unlikely to be found on the ocean. The energy exchange associated with the modulational instability[3,6] drives significant changes in the spectral amplitudes between one probe and the next, while both linear and nonlinear forecasts implicitly assume the spectrum remains unchanged throughout the propagation. Therefore, it is interesting to see that, although the amplitudes of the waves are not well predicted, the phases are matched very well for the nonlinear forecast.

ACKNOWLEDGEMENTS

RS gratefully acknowledges support by EPSRC grant EP/V012770/1 and a QJMAM Fund grant from the IMA. Research visits to the University of Plymouth by MG were supported by a QJMAM Fund grant from the IMA. DE acknowledges financial support from the Swiss National Science Foundation (Fellowship P2GEP2-191480). The authors thank Christopher Luneau and Hubert Branger from the IRPHE/Pytheas Aix Marseille University for their help during the experiments.

Appendix: Data tables

In this appendix we provide detailed tables of correlations and RMS errors for the synthetic and experimental forecasts considered in sections III and IV, respectively.

TABLE I. Mean correlations $\bar{\rho}$ over 20 realisations between synthetic simulated seas and forecasts based on linear (superscript L) and nonlinear (superscript N) forecasts. Subscripts i, j denote that measurements from probe i are used to forecast probe j. Significant wave height H_s ranges from 0.02 to 0.04, for three peak-sharpening parameters $\gamma = 1$, 3.3 and 7.

	$\gamma = 1$			$\gamma = 3.3$			$\gamma = 7$		
H_s	0.02	0.03	0.04	0.02	0.03	0.04	0.02	0.03	0.04
$\bar{\rho}^L_{1,2}$	0.9663	0.8498	0.7204	0.9802	0.9015	0.8012	0.9823	0.9274	0.8382
$\bar{\rho}^N_{1,2}$	0.9883	0.9432	0.8914	0.9933	0.9637	0.9297	0.9928	0.9704	0.9368
$\bar{\rho}^L_{1,3}$	0.8895	0.6375	0.4327	0.9373	0.7419	0.5323	0.9449	0.7930	0.6014
$\bar{\rho}^N_{1,3}$	0.9665	0.8736	0.7898	0.9838	0.9227	0.8391	0.9834	0.9311	0.8630
$\bar{\rho}^L_{1,4}$	0.8096	0.4499	0.2574	0.8656	0.5604	0.3176	0.9036	0.6314	0.3667
$\bar{\rho}^N_{1,4}$	0.9530	0.8071	0.7057	0.9660	0.8708	0.7392	0.9762	0.8700	0.7693

TABLE II. RMS errors from 20 realisations between synthetic simulated seas and forecasts based on linear (superscript L) and nonlinear (superscript N) forecasts. Subscripts $1, j$ denote that measurements from probe P_1 are used to forecast probe P_j, so that $E^L_{1,j} = \sqrt{E((P_j - \zeta_L)^2)}$ and $E^N_{1,j} = \sqrt{E((P_j - \zeta_N)^2)}$. Significant wave height H_s ranges from 0.02 to 0.04, for three peak-sharpening parameters $\gamma = 1$, 3.3 and 7.

	$\gamma = 1$			$\gamma = 3.3$			$\gamma = 7$		
H_s	0.02	0.03	0.04	0.02	0.03	0.04	0.02	0.03	0.04
$E^L_{1,2}$	0.0012	0.0039	0.0070	0.0010	0.0032	0.0060	0.0009	0.0028	0.0054
$E^N_{1,2}$	0.0006	0.0024	0.0044	0.0006	0.0019	0.0036	0.0006	0.0017	0.0034
$E^L_{1,3}$	0.0021	0.0061	0.0101	0.0018	0.0053	0.0092	0.0017	0.0048	0.0085
$E^N_{1,3}$	0.0009	0.0036	0.0061	0.0009	0.0028	0.0054	0.0009	0.0027	0.0050
$E^L_{1,4}$	0.0029	0.0074	0.0114	0.0026	0.0069	0.0112	0.0022	0.0064	0.0109
$E^N_{1,4}$	0.0011	0.0044	0.0072	0.0013	0.0037	0.0069	0.0011	0.0037	0.0066

TABLE III. RMS error for linear (superscript L) and nonlinear (superscript N) forecast for the three experimental cases M, J1, and J2. Subscripts i, j denote that measurements from probe i are used to forecast probe j.

	Case M	Case J1	Case J2
$E^L_{1,2}$	0.0074	0.0005	0.0040
$E^N_{1,2}$	0.0030	0.0005	0.0030
$E^L_{1,3}$	0.0133	0.0008	0.0083
$E^N_{1,3}$	0.0061	0.0009	0.0053
$E^L_{1,4}$	0.0187	0.0010	0.0090
$E^N_{1,4}$	0.0087	0.0010	0.0052

REFERENCES

[1]L. Abusedra and M. R. Belmont. Prediction diagrams for deterministic sea wave prediction and the introduction of the data extension prediction method. *Int. Shipbuild. Prog.*, 58(1):59–81, 2011.

[2]M. Al-Ani, M. Belmont, and J. Christmas. Sea trial on deterministic sea waves prediction using wave-profiling radar. *Ocean Eng.*, 207:107297, 2020.

[3]T. B. Benjamin and J. E. Feir. The disintegration of wave trains on deep water Part 1. Theory. *J. Fluid Mech.*, 27(03):417–430, 1967.

[4]E. Blondel, F. Bonnefoy, and P. Ferrant. Deterministic non-linear wave prediction using probe data. *Ocean Eng.*, 37(10):913–926, 2010.

[5]D. Clamond and D. Henry. Extreme water-wave profile recovery from pressure measurements at the seabed. *J. Fluid Mech.*, 903:R3, 2020.

[6]A. Chabchoub, B. Kibler, C. Finot, G. Millot, M. Onorato, J. Dudley, and A. Babanin. The nonlinear Schrödinger equation and the propagation of weakly nonlinear waves in optical fibers and on the water surface. *Ann. Phys.*, 361:490–500, 2015.

[7]N. Desmars, F. Bonnefoy, S. T. Grilli, G. Ducrozet, Y. Perignon, C. A. Guérin, and P. Ferrant. Experimental and numerical assessment of deterministic nonlinear ocean waves prediction algorithms using non-uniformly sampled wave gauges. *Ocean Eng.*, 212(January):107659, 2020.

[8]D. G. Dommermuth and D. K. Yue. A high-order spectral method for the study of nonlinear gravity waves. *J. Fluid Mech.*, 184(1987):267–288, 1987.

[9]G. Ducrozet, F. Bonnefoy, D. Le Touzé, and P. Ferrant. A modified High-Order Spectral method for wavemaker modeling in a numerical wave tank. *Eur. J. Mech. B/Fluids*, 34:19–34, 2012.

[10]A. Fisher, J. Thomson, and M. Schwendeman. Rapid deterministic wave prediction using a sparse array of buoys. *Ocean Engineering*, 228:108871, 2021.

[11]Z. Gao, Z. C. Sun, and S. X. Liang On two approaches to the third-order solution of surface gravity waves. *Phys. Fluids*, 33(9), 097101, 2021.

[12]S. T. Grilli, C.-A. Guérin, and B. Goldstein Ocean Wave Reconstruction Algorithms Based on Spatio-temporal Data Acquired by a Flash LIDAR Camera. *Proceedings of the Twenty-first International Offshore and Polar Engineering Conference. Maui, Hawaii, USA*, 275–282, 2011.

[13]C. A. Guérin, N. Desmars, S. T. Grilli, G. Ducrozet, Y. Perignon, and P. Ferrant. An improved Lagrangian model for the time evolution of nonlinear surface waves. *J. Fluid Mech.*, 876:527–

552, 2019.

[14] D. Henry and G. P. Thomas. Prediction of the free-surface elevation for rotational water waves using the recovery of pressure at the bed. *Phil. Trans. Roy. Soc. A*, 376:20170102, 2018.

[15] T. Hilmer and E. Thornhill. Observations of predictive skill for real-time Deterministic Sea Waves from the WaMoS II. *Ocean. 2015 - MTS/IEEE Washingt.*, pages 1–7, 2016.

[16] T. Hlophe, H. Wolgamot, A. Kurniawan, P. H. Taylor, J. Orszaghova, and S. Draper. Fast wave-by-wave prediction of weakly nonlinear unidirectional wave fields. *Appl. Ocean Res.*, 112:102695, 2021.

[17] M. Huchet, A. Babarit, G. Ducrozet, J. C. Gilloteaux, and P. Ferrant. Nonlinear deterministic sea wave prediction using instantaneous velocity profiles. *Ocean Eng.*, 220:108492, 2021.

[18] P. A. E. M. Janssen. *The Interaction of Ocean Waves and Wind*. Cambridge University Press, 2004.

[19] E. Kit and L. Shemer. Spatial versions of the Zakharov and Dysthe evolution equations for deep-water gravity waves. *J. Fluid Mech.*, 450:201–205, 2002.

[20] M. Klein, M. Dudek, G. F. Clauss, S. Ehlers, J. Behrendt, N. Hoffmann, and M. Onorato. On the deterministic prediction of water waves. *Fluids*, 5(1):1–19, 2020.

[21] J. G. Kusters, K. L. Cockrell, B. S. Connell, J. P. Rudzinsky, and V. J. Vinciullo. FutureWaves™: A real-time Ship Motion Forecasting system employing advanced wave-sensing radar. *Ocean. 2016 MTS/IEEE Monterey, OCE 2016*, 2016.

[22] J. G. Kusters, B. S. Connell, W. M. Milewski, V. J. Vinciullo, and R. Van Dijk. Wave characterization and timing using doppler radar - Update on the futurewaves™ wave and vessel motion forecasting system. *Ocean. 2019 MTS/IEEE Seattle.*, (October), 2019.

[23] Y. Law, H. Santo, K. Lim, and E. Chan. Deterministic wave prediction for unidirectional sea-states in real-time using Artificial Neural Network. *Ocean Eng.*, 195:106722, 2020.

[24] G. Li, G. Weiss, M. Mueller, S. Townley, and M. R. Belmont. Wave energy converter control by wave prediction and dynamic programming. *Renew. Energy*, 48:392–403, 2012.

[25] M. S. Longuet-Higgins and O. M. Phillips. Phase velocity effects in tertiary wave interactions. *J. Fluid Mech.*, 12(03):333–336, 1962.

[26] B. Molin, F. Remy, O. Kimmoun, and E. Jamois. The role of tertiary wave interactions in wave-body problems. *J. Fluid Mech.*, 528:323–354, 2005.

[27] M. Previsic, A. Karthikeyan, and D. Lyzenga. In-Ocean Validation of a Deterministic Sea Wave Prediction (DSWP) System leveraging X-Band Radar to Enable Optimal Control in Wave

Energy Conversion Systems. *Appl. Ocean Res.*, 114(July):102784, 2021.

[28]Y. Qi, G. Wu, Y. Liu, M.-H. Kim, and D. K. P. Yue. Nonlinear phase-resolved reconstruction of irregular water waves. *J. Fluid Mech*, 838:544–572, 2018.

[29]L. Shemer and A. Chernyshova. Spatial evolution of an initially narrow-banded wave train. *J. Ocean Eng. Mar. Energy*, 3(4):333–351, 2017.

[30]L. Shemer, H. Jiao, E. Kit, and Y. Agnon. Evolution of a nonlinear wave field along a tank: experiments and numerical simulations based on the spatial Zakharov equation. *J. Fluid Mech.*, 427:107–129, 2001.

[31]L. Shemer, E. Kit, and H. Jiao. An experimental and numerical study of the spatial evolution of unidirectional nonlinear water-wave groups. *Phys. Fluids*, 14(10):3380–3390, 2002.

[32]A. Simanesew, K. Trulsen, H. E. Krogstad, and J. C. Nieto Borge. Surface wave predictions in weakly nonlinear directional seas. *Appl. Ocean Res.*, 65:79–89, 2017.

[33]G. G. Stokes. On the theory of oscillatory waves. *Trans. Camb. Phil. Soc*, 8:441–455, 1847.

[34]R. Stuhlmeier and M. Stiassnie. Nonlinear dispersion for ocean surface waves. *J. Fluid Mech.*, 859:49–58, 2019.

[35]R. Stuhlmeier and M. Stiassnie. Deterministic wave forecasting with the Zakharov equation. *J. Fluid Mech.*, 913:1–22, 2021.

[36]K. Trulsen. Spatial Evolution Of Water Surface Waves. In *Fifth Int. Symp. WAVES 2005*, number 127, pages 1–10, 2005.

[37]G. Wang and Y. Pan. Phase-resolved ocean wave forecast with ensemble-based data assimilation. *J. Fluid Mech.*, 918:A19, 2021.

[38]B. J. West, K. A. Brueckner, R. S. Janda, D. M. Milder, and R. L. Milton. A new numerical method for surface hydrodynamics. *J. Geophys. Res.*, 92(C11):11803, 1987.

[39]G. Wu. Direct Simulation and Deterministic Prediction of Large-scale Nonlinear Ocean Wave-field. *MIT Ph.D. thesis*, (1994):258, 2004.

[40]A. Zavadsky, A. Benetazzo, and L. Shemer. On the two-dimensional structure of short gravity waves in a wind wave tank. *Phys. Fluids*, 29:016601, 2017.

[41]W. Zhao, P. H. Taylor, H. A. Wolgamot, and R. Eatock Taylor. Amplification of random wave run-up on the front face of a box driven by tertiary wave interactions. *J. Fluid Mech.*, 869:706–725, 2019.

[42]V. Zinchenko, L. Vasilyev, S. O. Halstensen, and Y. Liu. An improved algorithm for phase-resolved sea surface reconstruction from X-band marine radar images. *J. Ocean Eng. Mar.*

Energy, 7(1):97–114, 2021.